

This is the accepted manuscript made available via CHORUS. The article has been published as:

Correlations with projectile-like fragments and emission order of light charged particles

Z. Kohley, A. Bonasera, S. Galanopoulos, K. Hagel, L. W. May, A. B. McIntosh, B. C. Stein, G. A. Souliotis, R. Tripathi, S. Wuenschel, and S. J. Yennello

Phys. Rev. C **86**, 044605 — Published 4 October 2012

DOI: [10.1103/PhysRevC.86.044605](https://doi.org/10.1103/PhysRevC.86.044605)

Correlations with projectile-like fragments and emission order of light charged particles

Z. Kohley,^{1,2,3,*} A. Bonasera,^{2,4} S. Galanopoulos,² K. Hagel,² L. W. May,^{1,2} A. B. McIntosh,²
B. C. Stein,^{1,2} G. A. Souliotis,^{2,5} R. Tripathi,² S. Wuenschel,^{1,2} and S. J. Yennello^{1,2}

¹*Chemistry Department, Texas A&M University, College Station, Texas 77843, USA*

²*Cyclotron Institute, Texas A&M University, College Station, Texas 77843, USA*

³*National Superconducting Cyclotron Laboratory, Michigan State University, East Lansing, Michigan, 48824, USA*

⁴*Laboratori Nazionali del Sud, INFN, I-95123 Catania, Italy*

⁵*Laboratory of Physical Chemistry, Department of Chemistry,
National and Kapodistrian University of Athens, Athens 15771, Greece*

(Dated: September 20, 2012)

Correlations of mid-rapidity light charged particles (LCPs) and intermediate mass fragments (IMFs) with projectile-like fragments (PLFs) have been examined from the 35 MeV/u $^{70}\text{Zn} + ^{70}\text{Zn}$, $^{64}\text{Zn} + ^{64}\text{Zn}$, and $^{64}\text{Ni} + ^{64}\text{Ni}$ reaction systems. A new method was developed to examine the flow of the particles with respect to the PLF. The invariant PLF-scaled flow allowed for the dynamics of the mid-rapidity $Z = 1-4$ particles to be studied. Strong differences in the PLF-scaled flow were observed between the different isotopes. In particular, the most n-rich LCPs exhibited a negative PLF-scaled flow in comparison to the other LCPs. A classical molecular dynamics model and a 3-body Coulomb trajectory simulation were both used to show that the PLF-scaled flow observable could be connected to the average order of emission of the LCPs. The experimental results suggest that the mid-rapidity region is preferentially populated with neutron-rich LCPs and $Z = 3-4$ IMFs at a relatively early stage in the collision. The deuteron and ^3He particles are emitted later followed, lastly, by protons and alphas. The average order of emission of the mid-rapidity LCPs was extracted from the constrained molecular dynamics simulations and showed good agreement with the emission order suggested by the experimental PLF-scaled flow results.

PACS numbers: 25.70.-z, 25.70.Mn, 25.70.Pq

I. INTRODUCTION

Understanding the mechanisms responsible for particle production in the Fermi energy domain is an important task that could provide insights into the behavior and properties of nuclear matter. In the examination of peripheral and semi-peripheral intermediate energy heavy-ion collisions an important source of particle production has been found to originate from a mid-rapidity, or neck, region in between that of the projectile-like (PLF) and target-like (TLF) fragments [1–6]. Exploring the dynamics/mechanisms responsible for the formation of this neck-like source could provide information on the nucleon-nucleon interaction and nuclear Equation of State (EoS).

Two sources for particle production are often discussed in relation to these semi-peripheral heavy-ion collisions: (1) the decay of the excited quasi-projectile (QP) and quasi-target (QT) which, respectively, produce the PLF and TLF and (2) the emission of fragments from the break-up of a neck-like source produced at mid-rapidity in between the PLF and TLF. Experimental results have demonstrated an increased neutron to proton ratio (N/Z) of the mid-rapidity region in comparison to the quasi-projectile source through the examination of isotopically resolved fragments as well as the detection of

free neutrons [5–13]. For example, Lukasik *et al.* showed that 65-70% of the total triton production can be attributed to the mid-rapidity region in semi-peripheral reactions [5]. Furthermore, it has been suggested that the neck-like structure represents a low-density region of nuclear matter between the higher density QP and QT [14, 15]. Thus, the neck region can provide an opportunity to examine dilute neutron-rich nuclear matter. The study of this low-density asymmetric nuclear matter should provide observables sensitive to the nuclear EoS. Theoretical models have shown that the isospin content and production of intermediate mass fragments (IMFs) in the neck region could be used to probe the nuclear EoS [4, 16–18].

The mid-rapidity production mechanism suggests an important non-equilibrium or dynamical component of fragment formation in comparison to the binary deep-inelastic reaction mechanism [4]. Experimental and theoretical studies have indicated that the mid-rapidity particles are produced from a combination of complex mechanisms. Gingras *et al.* used a molecular dynamics simulations to show that the formation of the mid-rapidity particles could be attributed to both a prompt emission, due to nucleon-nucleon collisions, and a later emission from the tails of the QP and QT [19]. Similarly, 3-body Coulomb trajectory calculations showed that the production of mid-rapidity IMFs could be connected to both a fast emission from the neck region and a later emission from the surface of the QP or QT [20]. Experimental

* zkohley@gmail.com

studies by Hudan *et al.* [21] and McIntosh *et al.* [21, 22] suggested that QP is likely deformed after the collisions, which produces an asymmetric emission pattern focused towards the mid-rapidity region.

Since the mid-rapidity products are being produced from different mechanisms or sources it is of interest to explore the time-scale and order of their emission. Particle-particle correlations [23–25], velocity correlations [26–29], fission fragment angular distributions [30], and Coulomb proximity affects [21, 22, 31–33] have been used in attempts to extract information on the emission time of fragments. The proximity of the PLF and TLF to the mid-rapidity LCPs can be exploited to provide information on their emission time since particles emitted at early stages in the reaction will feel an increased Coulomb potential due to the increased proximity. In general, understanding the time and order of emission of LCPs and IMFs is important for improving our understanding of the fragmentation process in semi-peripheral collisions. More specifically, it is of interest to explore how the order of emission may change with the isospin concentration of the fragments as the average time of emission of LCPs has been predicted to be sensitive to the nuclear EoS [34]. Recently, both Hudan *et al.* [35] and De Filippo *et al.* [36] have presented experimental evidence indicating an earlier emission time for IMFs with increased neutron-to-proton ratios (N/Z).

In the following paper, the dynamics and fragmentation of the mid-rapidity region are investigated for isotopically identified LCPs and $Z = 3-4$ IMFs. Specifically, the correlations between the PLF and LCPs are explored and are shown to provide information on the average order of emission of LCPs, providing a complementary picture to the recent IMF results presented in Refs. [35] and [36]. Theoretical simulations are used to help validate the proposed relationship between the PLF-LCP correlations and average order of emission.

II. EXPERIMENT

The K500 Superconducting Cyclotron at the Texas A&M University Cyclotron Institute was used to produce beams of ^{70}Zn , ^{64}Zn , and ^{64}Ni at 35 MeV/nucleon which were collided with ^{70}Zn (95%), ^{64}Zn (99.8%), and ^{64}Ni (98.0%) self-supporting targets, respectively. The reaction products were collected using the 4π NIMROD-ISiS array (Neutron Ion Multi-detector for Reaction Oriented Dynamics with the Indiana Silicon Sphere) [37]. The entire charged particle array is housed inside the Texas A&M Neutron Ball [38], which provides an average neutron multiplicity.

The charged particle array consists of 14 concentric rings, labeled rings 2-15, ranging from 3.6° to 167.0° in lab. Rings 2-9, ranging from 3.6° to 45.0° , had the same geometry as the INDRA detector [39] and rings 10-15 were of the ISiS geometry [40]. Rings 2-9 each consisted of 10 single telescope modules and 2 super telescope mod-

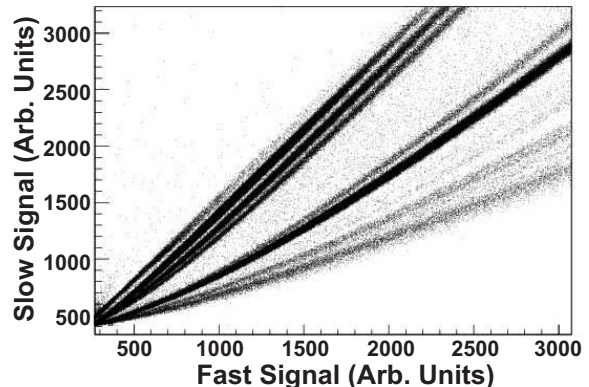


FIG. 1. Typical experimental plot of the slow versus fast components from the CsI(Tl)-PMT signal.

ules. A single telescope module contained a $150\mu\text{m}$ or $300\mu\text{m}$ silicon detector placed in front of a thallium doped cesium iodide crystal, CsI(Tl). The super telescopes had both a $150\mu\text{m}$ and $500\mu\text{m}$ Si placed in front of the CsI(Tl) crystal. Rings 10 and 11 each had 18 single telescope modules with $300\mu\text{m}$ Si-CsI(Tl) detectors. Rings 12-15 each contained 18 single telescope modules with a $500\mu\text{m}$ thick silicon detector in front of the CsI.

Three methods of particle identification are available in the NIMROD-ISiS array. In rings 2-11 pulse shape analysis of the CsI(Tl)-PMT (thallium doped cesium-iodide with a photomultiplier tube) signals allowed for isotopic identification of light charged particles, $Z = 1-2$. As shown in Fig. 1, clear separation of neutron/gamma, proton, deuteron, triton, ^3He , and alpha particles is observed. Isotopic resolution of heavier mass fragments was achieved through ΔE -E plots from the Si-CsI (single telescope), shown in Fig. 2, and Si-Si (super telescope) modules. In the forward angle rings isotopic resolution of $Z = 1-17$ particles and elemental resolution up to the charge of the beam was obtained through the Si-CsI and Si-Si detector modules. Detector thresholds limited the isotopic resolution to $Z = 1-2$ particles for the backward angles.

A linearization procedure was utilized to complete the particle identification [37, 41]. This provided a 1-D distribution from the 2-D plots. An example of a linearized Si-CsI plot is shown in Fig. 3 for the $Z = 12-15$ fragments, where the linearization distance is labeled as $LinZ$. The most prominent isotope of each elemental band are labeled accordingly. Each isotope was fit with a Gaussian function defined as

$$G(x) = C \cdot e^{-0.5 \cdot \left(\frac{x-\mu}{\sigma}\right)^2} \quad (1)$$

where C is the height, μ is the center, and σ defines the width of the Gaussian. The parameters for each individual Gaussian were determined by minimizing the error

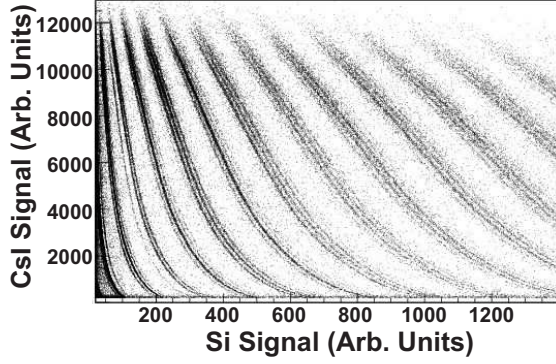


FIG. 2. Typical experimental ΔE - E plot showing the CsI(Tl)-PMT signal plotted against a $500\mu\text{m}$ silicon signal. The data extends to channel 4000 on the Si axis. An expanded view is presented to demonstrate the isotopic resolution.

between the sum of the Gaussians and the experimental data for each element. One of the main advantages of fitting the 1-D projections with Gaussian functions, rather than setting hard limits to define each isotope, is that the accuracy of the isotopic identification can be quantified. The percent contamination for a given $LinZ$ value was calculated for each particle as

$$\%Contam = \frac{\left(\sum_{i=0}^{N_{Gauss}} G_i(LinZ) \right) - G_{Max}(LinZ)}{G_{Max}(LinZ)} \quad (2)$$

where N_{Gauss} is the number of Gaussian functions used for the given element, $G_i(LinZ)$ is the value of the i^{th} Gaussian at the point $LinZ$, and $G_{max}(LinZ)$ representing the maximum $G_i(LinZ)$ from all the Gaussians. The mass of each particle was defined by the A of the Gaussian which had the maximum value, $G_{max}(LinZ)$, for the $LinZ$ associated with the particle. If the $\%Contam \leq 20\%$ then the mass identification of the particle was used in the following analysis. If $\%Contam > 20\%$ the particle was considered to be elementally identified only.

The silicon and CsI detectors were calibrated in order to determine the total kinetic energy of each detected particle. The relationship derived by Tasson-Got [42] was used to relate the light output from the CsI to the particle energy. Proton (30 and 55 MeV), deuteron (60 MeV), and alpha (100 MeV) calibration beams were collected in order help constrain the parameters of the CsI calibration. The punch-through energies of the identified fragments, a ^{228}Th source, and a 500 MeV ^{20}Ne calibration beam, were used to constrain the silicon detector calibrations. The final energy spectra were compared to

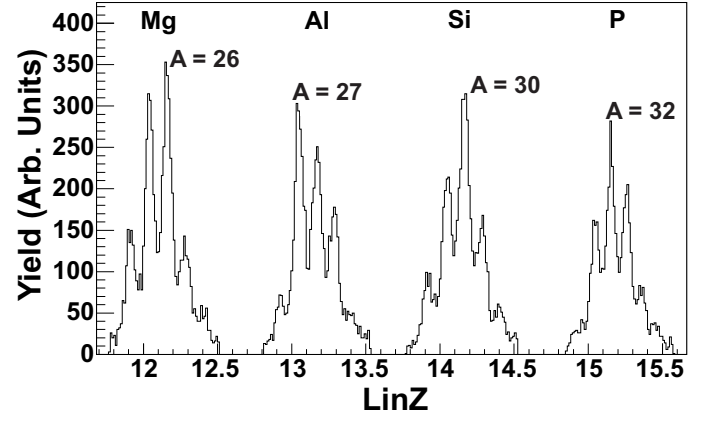


FIG. 3. Experimental 1-D projection of Si-CsI plot for the $Z = 12-15$ elemental band. The most prominent isotope of each element is labeled.

previous NIMROD data sets for 35 MeV/nucleon systems of similar size and showed excellent agreement [43, 44].

III. EVENT CLASSIFICATION

Peripheral collisions can often be characterized by the formation of a projectile-like and target-like fragment along with light charged particles. In examining the neck emission process it is important to separate events according to a consistent ordering parameter since the size and mechanisms of the mid-rapidity region may change from the most central to peripheral collisions [5]. In the following analysis, the charge (Z) of the PLF is used for event classification. For each event, the PLF was selected as the heaviest detected fragment with a positive center-of-mass velocity. In central collisions the heaviest detected fragment may not truly represent a “projectile-like” fragment yet can still provide event classification. The focus of this paper is on the results from PLFs with a charge near to that of the projectile. Furthermore, all events must have passed the criterion that the total detected charge for each event ($SumZ$) be greater than 40% of the charge of the total system. This helped improve the event classification by eliminating events in which the PLF was not actually detected in the NIMROD-ISiS array.

Molecular dynamics simulations were used to examine the correlation between the PLF Z and the reduced impact parameter, defined as $b_{red} = b/b_{max}$. The value of b_{max} was taken as $1.2(A_{proj}^{1/3} + A_{tgt}^{1/3})$. In Fig. 4 the reduced impact parameter for each simulated event is plotted against the charge of the PLF from the constrained molecular dynamics, CoMD, simulation [45, 46] (refer to Section V. for a description of CoMD). The results shown have been filtered using a software replica of the NIMROD-ISiS array and the $SumZ$ criterion has been applied. An almost linear relationship between the

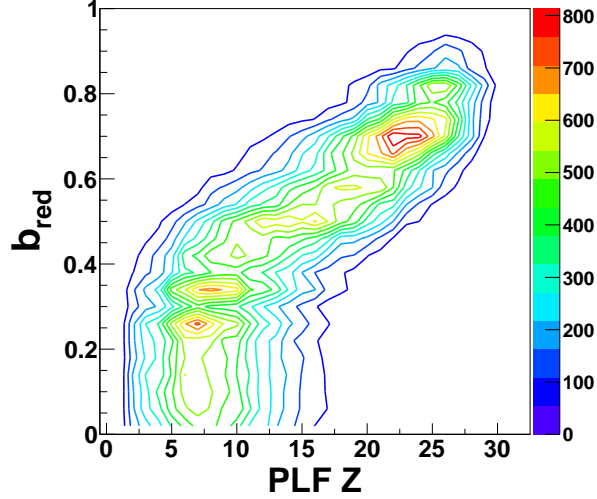


FIG. 4. (color online) Contour plot depicting the relationship between the charge of the detected PLF and the reduced impact parameter, b_{red} , for the $^{70}\text{Zn} + ^{70}\text{Zn}$ reaction from the CoMD simulation.

PLF Z and b_{red} is observed for PLFs with $Z = 15$ -30. Thus, selecting events by the charge of the PLF, for PLFs with $Z > 15$, should provide a relatively well-defined impact parameter selection. Below a PLF Z of about 15 it appears that the heaviest detected fragment can be associated with a wide variety of impact parameters.

The relationship between the azimuthal angle of the PLF and the reaction plane was also examined. For very peripheral collisions, where the PLF charge is close to that of the projectile, the azimuthal angle of the PLF should be strongly correlated with the reaction plane angle. The difference between the reaction plane and PLF azimuthal angle, $\Delta\phi_{PLF-RxnPlane}$, is shown as a function of the PLF charge in Fig. 5 from the CoMD simulation. This correlation is again examined using the filtered molecular dynamics simulations, in which the known reaction plane can be compared to the azimuthal angle of the PLF. The results demonstrate that the average $\Delta\phi_{PLF-RxnPlane}$ is almost perfectly anti-aligned (180°) from the reaction plane. The 180° anti-alignment with the reaction plane is due to the dominance of the attractive mean-field below the balance energy [47, 48] causing the projectile to stick and rotate around the target. Figs. 4 and 5 demonstrate that selecting classes of events by the charge of the PLF provides both an impact parameter selection as well as a correlation with the reaction-plane for PLFs with $Z \gtrsim 15$.

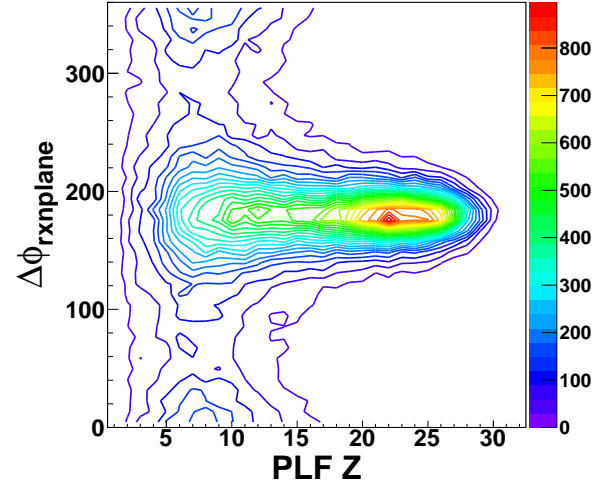


FIG. 5. (color online) Contour plot depicting the relationship between the charge of the detected PLF and the difference between the reaction plane and PLF azimuthal angle, $\Delta\phi_{PLF-RxnPlane}$. Results are shown from the filtered CoMD simulation for the ^{70}Zn system.

IV. EXPERIMENTAL RESULTS

A. PLF-scaled Flow

The correlation between the PLF and LCPs has been investigated through a transverse flow type analysis. In heavy-ion collisions, transverse flow has been commonly studied by plotting the average fragment momentum in the reaction plane as a function of rapidity. In the following, the average momentum of the LCPs *in the plane of the PLF*, $\langle p_x \rangle$, was calculated and examined as a function of the fragment rapidity. This then allows for the correlation, or movement, of the LCPs with respect to the PLF to be investigated.

In order to compare transverse flow results at a variety of energies Bonasera and Csernai used a scale-invariant flow analysis [49]. Similarly, in order to examine the correlations between the LCPs and PLF different scalings of the PLF-plane momentum ($\langle p_x \rangle$) and rapidity (Y) of the fragments were investigated. The different scaling analyses are discussed below and a comparison of each method is presented in Fig. 6.

Following the work of Bonasera and Csernai [49] the fragment properties can be scaled as,

$$p_x^{Proj||} = \frac{p_{x,frag}/A_{frag}}{p_{||,proj}^{cm}/A_{proj}} \quad (3a)$$

$$Y^{Proj||} = \frac{Y_{frag}^{cm}}{Y_{proj}^{cm}} \quad (3b)$$

where $p_x^{Proj||}$ is the PLF-plane momentum per nucleon of the fragment ($p_{x,frag}/A_{frag}$) scaled by the parallel

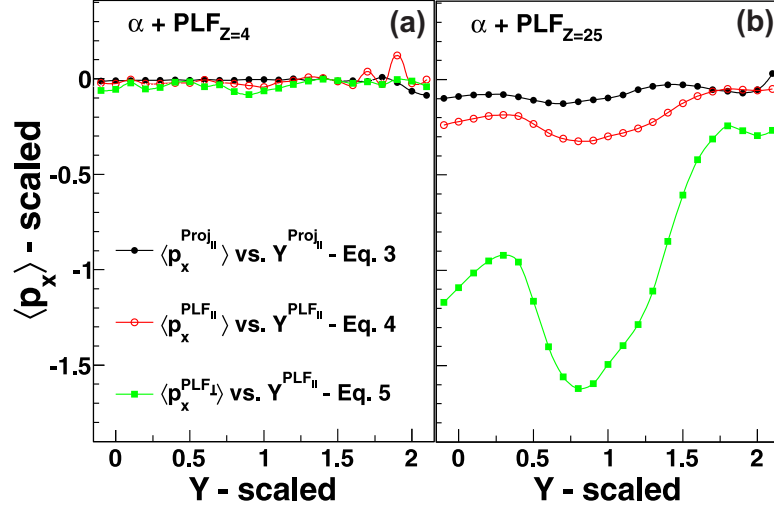


FIG. 6. (color online) Average scaled PLF-plane momentum, $\langle p_x \rangle$, of alpha particles in correlation with $Z = 4$ (a) and $Z = 25$ (b) PLFs is shown as a function of the scaled rapidity (Y). The presented results are from the 35 MeV/nucleon $^{70}\text{Zn} + ^{70}\text{Zn}$ system. The scaled momentum and rapidity have been calculated as described in Eqs. 3-5.

momentum per nucleon of the projectile in the center-of-mass ($p_{||,proj}^{cm}/A_{proj}$). Y^{Proj} represents the fragment center-of-mass rapidity (Y_{frag}^{cm}) scaled by the center-of-mass rapidity of the projectile (Y_{proj}^{cm}). This scaling, as mentioned, was originally used to compare the flow at different energies and therefore is sensitive to the kinematics of the projectile rather than the PLF.

In order to account for the PLF properties, $p_x^{PLF_{||}}$ and $Y^{PLF_{||}}$ were calculated as

$$p_x^{PLF_{||}} = \frac{p_{x,frag}/A_{frag}}{p_{||,PLF}^{cm}/A_{PLF}} \quad (4a)$$

$$Y^{PLF_{||}} = \frac{Y_{frag}^{cm}}{Y_{PLF}^{cm}} \quad (4b)$$

with the PLF-plane fragment momentum scaled by the parallel momentum of the PLF ($p_{||,PLF}^{cm}/A_{PLF}$) and the rapidity of the fragment scaled by the PLF rapidity (Y_{PLF}^{cm}). Both $p_x^{PLF_{||}}$ and $Y^{PLF_{||}}$ are invariant with respect to kinematics of different PLFs.

Lastly, a transverse PLF scaling, $p_x^{PLF_{\perp}}$, was calculated as,

$$p_x^{PLF_{\perp}} = \frac{p_{x,frag}/A_{frag}}{p_{\perp,PLF}^{cm}/A_{PLF}} \quad (5)$$

where the PLF-plane transverse momentum of the fragment is scaled by the transverse momentum of the PLF ($p_{\perp,PLF}^{cm}/A_{PLF}$). The average $\tilde{p}_x^{PLF_{\perp}}$ was plotted against the $Y^{PLF_{||}}$ from Eq. 4, as shown in Fig 6. The transverse scaling is PLF-invariant since both $p_x^{PLF_{\perp}}$ and $Y^{PLF_{||}}$ are scaled relative to the properties of the PLF.

The discussed scalings, Eqs. 3-5, are compared in Fig. 6 for the correlation of alpha particles with both a $Z = 4$

and $Z = 25$ PLF. The results for the $Z = 4$ PLFs and alpha particles show a constant $\langle p_x \rangle = 0$, which demonstrates no significant correlations. A $\langle p_x \rangle = 0$ is representative of a random emission of alpha particles with respect to the $Z = 4$ PLF. In contrast, strong correlations are observed between the $Z = 25$ PLF demonstrating that the emission of the alpha particles is affected by the PLF.

From Fig. 6, it is clear that the choice of scaling method has a distinct effect on the shape of the $\langle p_x \rangle$ vs. Y plot. The scaling by the projectile kinematics, defined in Eq. 3, shows the weakest correlations between the alpha particle and $Z = 25$ PLF. In comparison the parallel PLF scaling, Eq. 4, shows a distinct decrease, or dip, in the $\langle p_x \rangle$ around $Y = 1$. This indicates a correlation, or interaction, between the alpha particles and PLF when they have a similar rapidities.

In examining the results from the Eq. 5 scaling (PLF_{\perp}) two distinct regions are now present. A mid-rapidity region ranging from $0.0 \leq Y \leq 0.45$ and a PLF region from $0.5 \leq Y \leq 1.5$, in which there appears to be a Coulomb-dip due to the alpha particle interaction with the PLF. While these features are also present in the $PLF_{||}$ scaling of Eq. 4, they are more prominent with the transverse PLF scaling. It is interesting to note that the strongest correlations appear when the alpha particle PLF-plane momentum was scaled relative to the transverse momentum of the PLF. If the observed PLF-plane momentum of the alpha particles had been simply due to the inherent transverse motion of the PLF, the strong correlations observed in Fig. 6 would be diminished by the PLF_{\perp} scaling. Thus, it appears that the transverse PLF scaling helps remove the inherent transverse momentum of the event and allows for the correlation between the fragment and PLF to become more pronounced.

The following analysis is performed using the scaling of Eq. 5 with $\langle p_x^{PLF\perp} \rangle$ and $Y^{PLF\parallel}$. For simplicity the scaled fragment momentum and rapidity, from Eq. 5, will be denoted as $\langle \tilde{p}_x \rangle$ and the scaled rapidity as \tilde{Y} , respectively. Additionally, this analysis will be referred to as the *PLF-scaled flow*, since it represents the scaled flow of the particles with respect to the PLF.

B. Mid-Rapidity Slope

The slope of the $\langle \tilde{p}_x \rangle$ over the mid-rapidity region, denoted as $\partial \langle \tilde{p}_x \rangle / \partial \tilde{Y}$, can provide information about the movement of the fragments with respect to the PLF [50, 51]. For example, a positive slope would indicate that the closer the fragment is to the PLF, the more strongly it's motion is correlated with the PLF direction. In order to investigate the movement of the mid-rapidity fragments a linear fit was applied to the $\langle \tilde{p}_x \rangle$ vs. \tilde{Y} plot from $-0.1 \leq \tilde{Y} \leq 0.45$. The fit could not be extended to $\tilde{Y} < -0.1$ due to increased detector thresholds at backward angles. Fig. 7 presents the $\langle \tilde{p}_x \rangle$ as a function of \tilde{Y} for protons, deuterons, and tritons in correlation with $Z = 24$ PLFs. The linear fit is shown as the solid line for each isotope. The slope of the linear fit is then used to quantify the PLF-scaled flow for the different particle types.

A negative offset from zero in $\langle \tilde{p}_x \rangle$ is present for the $Z = 1$ fragments of Fig. 7. This offset is not unexpected, as $\langle \tilde{p}_x \rangle$ would only pass through zero if calculated with respect to the reaction plane. While the PLF plane is correlated with the reaction plane, significant deviations are indicated from the CoMD simulation in Fig. 5. Thus, the negative offset can be attributed to the reaction plane dispersion, which should not affect the extracted slope [52–54].

The PLF-scaled flow results suggest that the mid-rapidity protons, deuterons, and tritons are moving in different directions with respect to the PLF. The positive slope exhibited by the protons would imply that they are, on average, moving in alignment with the PLF. In contrast, the tritons appear to move in the opposite directions, away from the PLF, implied by the negative slope or PLF-scaled flow.

The mid-rapidity slope ($\partial \langle \tilde{p}_x \rangle / \partial \tilde{Y}$) was extracted for the protons, deuterons, and tritons in correlation with PLFs of charge $Z = 3$ to $Z = 30$. In Fig. 8, the extracted slopes are plotted as a function of the charge of the PLF. The results demonstrate that beyond a PLF Z of about 20 the magnitude and sign of the proton, deuteron, and triton slopes are drastically different. In particular, the difference increases with increasing charge, or size, of the PLF. As indicated by the linear fits, the extracted slopes suggest that the protons, deuterons, and tritons have different trajectories relative to the PLF. These results indicate very different dynamics for the different $Z = 1$ isotopes.

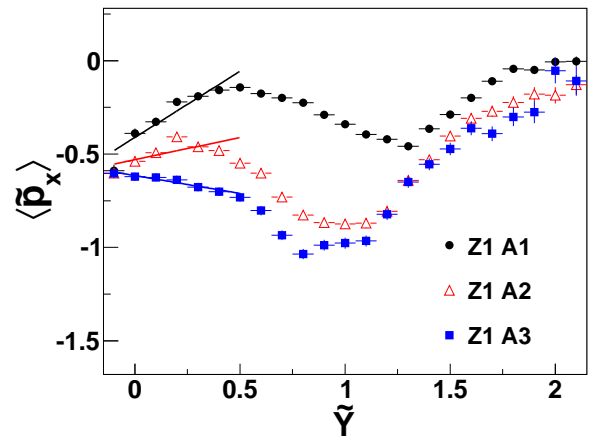


FIG. 7. (color online) The average scaled PLF-plane momentum, $\langle \tilde{p}_x \rangle$, of protons, deuterons, and tritons is shown as a function of the scaled rapidity, \tilde{Y} , from the $^{70}\text{Zn} + ^{70}\text{Zn}$ system. The solid lines represent linear fits over the range $-0.1 \leq \tilde{Y} \leq 0.45$.

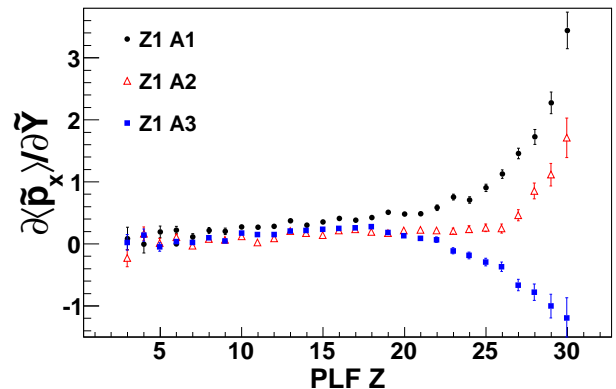


FIG. 8. (color online) The slope of the mid-rapidity particles, $\partial \langle \tilde{p}_x \rangle / \partial \tilde{Y}$, shown as a function of the PLF charge for protons, deuterons, and tritons. The data are from the $^{70}\text{Zn} + ^{70}\text{Zn}$ system.

C. Order of Emission

We propose that the different trajectories of the mid-rapidity fragments, shown in Fig. 8 are connected to their proximity to the PLF and TLF at their time of emission. Fig. 9 presents a simplified illustration of the possible effect of the PLF-TLF proximity to the mid-rapidity fragments. If the mid-rapidity fragment is emitted while in a close proximity to the PLF and TLF (left side of Fig. 9) then the Coulomb potential would likely force the fragment trajectory to be anti-aligned, or perpendicular, with the PLF-TLF axis. This would result in a negative slope of the $\langle \tilde{p}_x \rangle$. If the formation of the fragment occurs at a later time, where the PLF-TLF proximity is decreased, then it is possible for a more aligned emission to occur (right side of Fig. 9). Particles following the trajectory

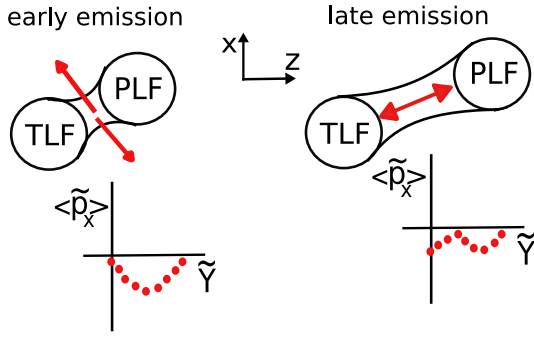


FIG. 9. (color online) Simple illustration demonstrating the proposed PLF-TLF proximity effect on the mid-rapidity fragments. The left side depicts the mechanism producing negative slopes due to an early emission of fragments. The right side shows a later emission of mid-rapidity fragments producing a positive slope.

of the PLF would produce a positive slope value or PLF-scaled flow. In this context, the results from Fig. 8 would suggest that the average order of emission for the mid-rapidity $Z = 1$ isotopes is $\tau_t < \tau_d < \tau_p$, where τ is the average time of emission, since $\partial \langle \tilde{p}_x \rangle / \partial \tilde{Y}$ decreases from the protons to deuterons to tritons.

In order to improve statistics for the extracted PLF-scaled flow, events were combined producing bins representing a selection of PLFs based on their charge, as shown in Fig. 10. The binning of the events does not change the overall trends observed in the PLF-scaled flow for the $Z = 1$ isotopes. Combining the events with different PLFs is possible since the scaling used (Eq. 5) is invariant to the PLF.

As previously mentioned, it is important to note that the separation between the proton, deuteron, and triton slopes increases with an increasing PLF charge. This may be understood by the increased Coulomb force that would be imparted on the mid-rapidity fragments from a higher PLF charge. Thus, events with a larger PLF Z should be more sensitive to the average order of emission of the particles.

The PLF-scaled flow of the $Z = 1$ isotopes are compared between the $^{70}\text{Zn} + ^{70}\text{Zn}$, $^{64}\text{Zn} + ^{64}\text{Zn}$, and $^{64}\text{Ni} + ^{64}\text{Ni}$ systems in Fig. 10(a). The results from all three systems are not presented for the $Z = 2$ isotopes because the error bars, from the linear fits, were larger than the differences between the systems. The results for the $Z = 1$ isotopes show that the PLF-scaled flow of the fragments is sensitive to the colliding system. The absolute magnitude of the slope was the largest for the ^{64}Zn ($N/Z = 1.13$) system followed by the ^{64}Ni ($N/Z = 1.28$) and then ^{70}Zn ($N/Z = 1.33$) systems. This demonstrates a dependence on the neutron to proton ratio of the colliding system where the PLF-scaled flow decreases with an increasing N/Z .

In Fig. 10(b) the slopes extracted from the $Z = 2$ isotopes are shown. Following the argument connecting the magnitude and sign of the slope to the average order of

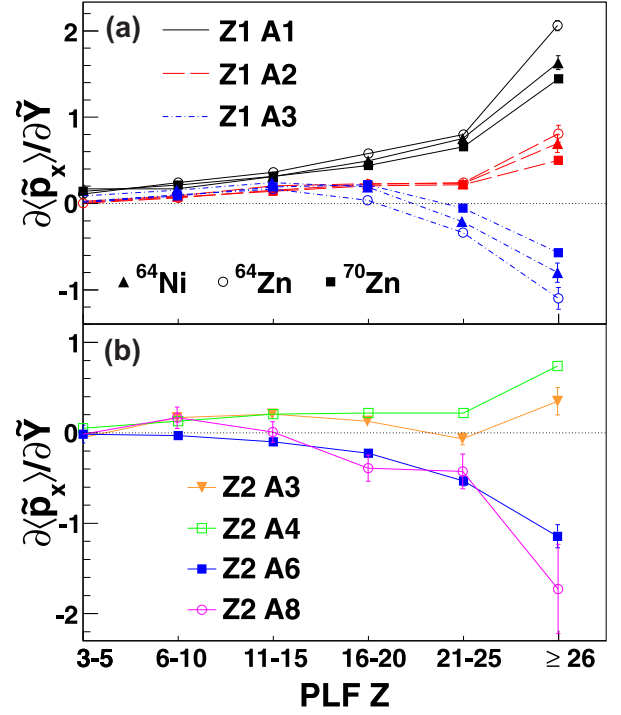


FIG. 10. (color online) The extracted slopes, $\partial \langle \tilde{p}_x \rangle / \partial \tilde{Y}$, for the $Z = 1$ (a) and $Z = 2$ (b) isotopes, are shown as a function of the binned PLF charge. Results from the 35 MeV/u $^{70}\text{Zn} + ^{70}\text{Zn}$, $^{64}\text{Zn} + ^{64}\text{Zn}$, and $^{64}\text{Ni} + ^{64}\text{Ni}$ systems are presented for the $Z = 1$ isotopes. Results from the $Z = 2$ isotopes are shown only from the $^{70}\text{Zn} + ^{70}\text{Zn}$ system.

emission, the results suggest that the ^6He and ^8He fragments are on average emitted in the early stages of the collision followed by the ^3He fragments and then alpha particles.

The $Z = 1$ and $Z = 2$ results show that the most neutron rich isotopes (triton, ^6He , ^8He) are on average formed early in the mid-rapidity region in comparison to the more proton-rich isotopes. This is likely related to the formation of a neutron-rich neck region. As mentioned, previous studies have shown an increased N/Z content in the neck region [5–11] and these results suggest that this may be connected to the preferential emission of the most neutron rich LCPs into that region during the early stages of the reaction process.

In Fig. 11 the extracted slopes from the PLF-scaled flow are combined for each element. The $Z = 1$ and $Z = 2$ results show an increasing positive PLF-scaled flow as a function of the PLF charge. This would suggest that all the $Z = 1$ and $Z = 2$ fragments have a relatively late emission time, which produces the positive slopes. However, when examining the $Z = 1$ and $Z = 2$ isotopes separately (Fig. 10) it is clear that the dynamics can vary widely and that the elemental results are dominated by the proton ($Z = 1$) and alpha ($Z = 2$)

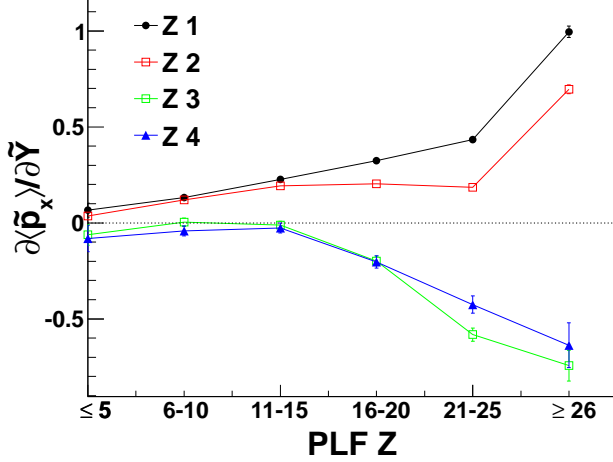


FIG. 11. (color online) The extracted slopes, $\partial \langle \tilde{p}_x \rangle / \partial \tilde{Y}$, for the $Z = 1, 2, 3$ and 4 fragments shown as a function of the binned PLF charge. Results are from the $35 \text{ MeV/u } ^{70}\text{Zn} + ^{70}\text{Zn}$ system.

particle trajectories.

The PLF-scaled flow was also investigated for the $Z = 3$ and $Z = 4$ fragments, as shown in Fig. 11, as a function of the PLF binned charge. The results for the $Z = 3$ (^6Li , ^7Li , ^8Li) and $Z = 4$ (^7Be , ^9Be , ^{10}Be) isotopes all showed identical PLF-scaled flows within the statistical uncertainties and, therefore, only the elemental results are shown. Based on the proposed arguments, the results imply that the mid-rapidity $Z = 3$ and $Z = 4$ fragments have, on average, a relatively early emission time since they exhibit a strong negative PLF-scaled flow. This begins to present a scenario in which the fragments commonly observed to have an increased mid-rapidity production (such as the triton, ^6He , $Z = 3$ and $Z = 4$ fragments) are also being produced on a relatively early time scale.

D. PLF Velocity Gates

Additional evidence that the extracted slope, or PLF-scaled flow, is connected to the average emission order is presented in Fig. 12. In each PLF charge bin, the PLFs were gated on their velocity relative the projectile velocity (V_{proj}). Then the PLF-scaled flow was extracted for the alpha particles from each PLF velocity gate. If the extracted slope is correlated to the proximity of the PLF and TLF, then a decreased slope would be expected for events in which the PLF velocity is dampened, since the PLF (and likely TLF) would separate slower. Therefore, the mid-rapidity particles would be in closer proximity to the PLF-TLF and have a decreased PLF-scaled flow due to the increased Coulomb potential. Similarly, when the PLF is moving at a faster velocity (near that of the projectile), the PLF and TLF would separate much quicker

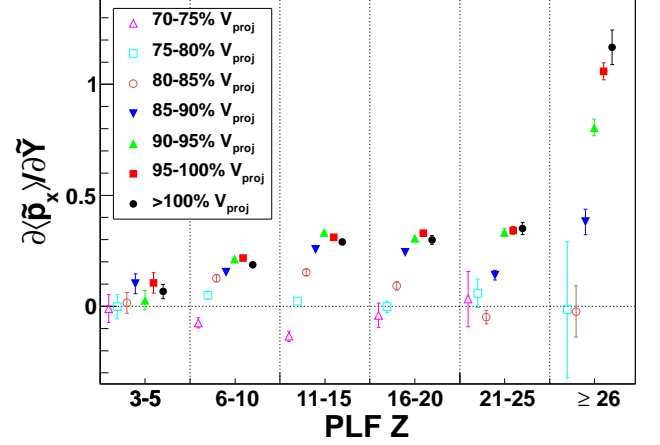


FIG. 12. (color online) The extracted slopes, $\partial \langle \tilde{p}_x \rangle / \partial \tilde{Y}$, for alpha particles are shown as a function of both the velocity and charge of the PLF. In each PLF charge bin the slope was extracted from events in which the velocity of the PLF was within a certain percentage of the velocity of the projectile, as described in the legend.

and the proximity to the mid-rapidity particles would be decreased. Thus, an increased PLF-scaled flow would be expected.

As shown in Fig. 12, a strong correlation is observed between the PLF velocity and the extracted PLF-scaled flow for the alpha particles. The PLF-scaled flow shows a clear increase with increasing PLF velocity. Negative slopes are even extracted for some of the most dampened events, in which the PLF velocity is 70-75% of the projectile velocity. Since the PLF-TLF separation is much slower for these dampened events, the negative slopes should be representative of a strong proximity of the PLF to the alpha particles. The largest effects were observed in the $Z \geq 26$ PLF bin, which would produce the strongest Coulomb interaction.

The results presented in Fig. 12 provided experimental evidence that the extracted slope from the PLF-scaled flow can be connected to the proximity of the PLF and TLF to the mid-rapidity particles. In combination with the results from Figs. 10 and 11 it appears that the average order of emission for the mid-rapidity $Z = 1$ fragments follows $\tau_t < \tau_d < \tau_p$ and the order for the mid-rapidity $Z = 2$ fragments is $\tau_{8\text{He}} \leq \tau_{6\text{He}} < \tau_{3\text{He}} < \tau_\alpha$. Additionally, the $Z = 3$ and $Z = 4$ PLF-scaled flows imply a relatively earlier emission during the reaction process.

V. THEORETICAL SIMULATIONS

While the experimental data suggests a connection between the PLF-scaled flow and average order of emission of the mid-rapidity fragments it is important to explore this idea in the context of simulations where the PLF-

TLF proximity, strength of the Coulomb potential, and time of fragment formation can be examined.

A. Coulomb Trajectory

The Coulomb trajectory of mid-rapidity particles was examined through a Monte Carlo simulation in which the proximity of the PLF and TLF was varied. A depiction of the Coulomb trajectory simulation is shown in Fig. 13. The initial configuration consisted of particle placed directly in between the PLF and TLF. The PLF and TLF were described by a sphere containing 30 protons with a radius of 4.9 fm, which is representative of a ^{70}Zn projectile. In the simulation, the PLF (TLF) was propagated at a velocity of $0.13 v/c$ with a center-of-mass angle of $\theta_{cm} = 13^\circ$ (193°), which corresponds to moving at the center-of-mass velocity of the 35 MeV/u ^{70}Zn projectile and entering the forward most ring of the NIMROD-ISiS array. The velocity vector of the mid-rapidity particle was randomly determined from a Maxwell-Boltzmann distribution with $T = 6$ MeV (the results did not depend significantly on the value of T). However, the x-component of the velocity (v_x) was adjusted such that the center-of-mass angle of the mid-rapidity particles (θ_{cm}) was similar to that of the PLF or TLF. Thus, the initial trajectories present a scenario in which a mid-rapidity particle is emitted in alignment with the motion of the PLF or TLF. The dashed red line represents the average initial trajectory of the mid-rapidity particles.

After determining the initial conditions for the simulation the mid-rapidity fragment, PLF, and TLF were propagated for 200 fm/c. The trajectories of the PLF and TLF, shown as the solid black lines, were propagated along their initial trajectory. The mid-rapidity fragment was propagated within the Coulomb field produced by the PLF and TLF, which is represented by the contour lines in Fig. 13. The simulation was carried out 5500 times in order to obtain the average trajectory of the mid-rapidity particles. After propagation for 200 fm/c the final PLF-plane momentum and scaled rapidity for each particle was calculated in order to examine the PLF-scaled flow for the different initial PLF-TLF proximities.

The results from the Coulomb trajectory simulation, shown in Fig. 14, demonstrate the strong effect that the proximity of the PLF-TLF can have on the trajectory of the mid-rapidity fragments and therefore, the extracted slope. When the distance of the PLF and TLF from the mid-rapidity particle was small, 15-25 fm, the strong Coulomb potential forces the particle to move perpendicular to the PLF-TLF axis producing a negative slope. As the distance of the PLF and TLF from the mid-rapidity particle is increased the initial trajectory of the particle is disturbed less by the Coulomb field and the strong negative flow is diminished. For example at a PLF-TLF distance of 45-50 fm the slope becomes very similar to positive slope that would be extracted from the initial trajectory of the particles, shown as open circles.

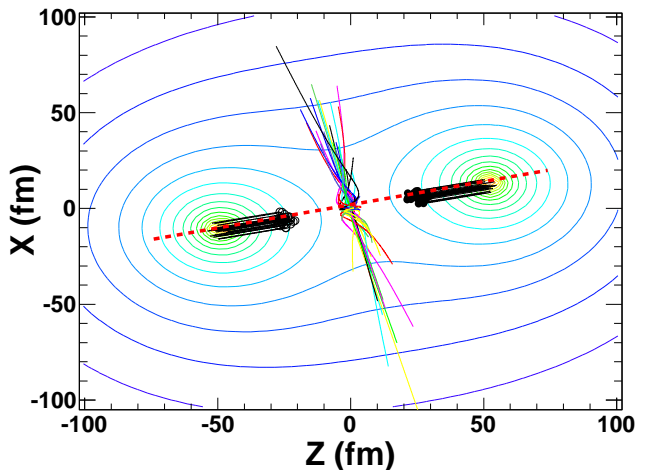


FIG. 13. (color online) Trajectories of the PLF, TLF, and mid-rapidity particles are shown from the Coulomb trajectory calculations in which the initial distance of the PLF and TLF was 25 fm from the mid-rapidity particle. The initial position of the PLF (TLF) is shown as the black filled (open) circles and the solid black lines represent the trajectory of the PLF (TLF). The contour lines depict the Coulomb potential produced from the final position of the PLF and TLF. The trajectories of the mid-rapidity particles are shown as solid lines originating from the (0,0) position. For clarity only 50 of the 5500 mid-rapidity particle trajectories are shown. The red dashed line represents the average initial trajectory of the mid-rapidity particles under no influence of the PLF-TLF Coulomb field.

The Coulomb trajectory results demonstrated that in a simple scenario, in which the nuclear force is neglected, the mid-rapidity particle trajectory is strongly affected by the proximity of the PLF and TLF. Both the positive and negative PLF-scaled flows from the experiment were qualitatively reproduced through varying the distance of the PLF and TLF from the particle.

B. Classical Molecular Dynamics (CMD)

The classical molecular dynamics (CMD) model [55, 56] provides a more sophisticated simulation than the Coulomb trajectory calculation in which the nuclear force, nucleon-nucleon collisions, and dynamical particle production is included. The CMD model was used to simulate the 35 MeV/u $^{70}\text{Zn} + ^{70}\text{Zn}$ reactions up to a time of 400 fm/c. The CMD results were filtered with a software replica of the NIMROD-ISiS array which accounts for geometry and energy thresholds of the detector.

Unlike the Coulomb trajectory calculation, the proximity of the PLF and TLF cannot be varied at the time of emission of the mid-rapidity particles in the CMD model since it is a dynamical simulation in which the particle emission is occurring throughout the reaction. Therefore, in order to investigate the affect of the Coulomb potential

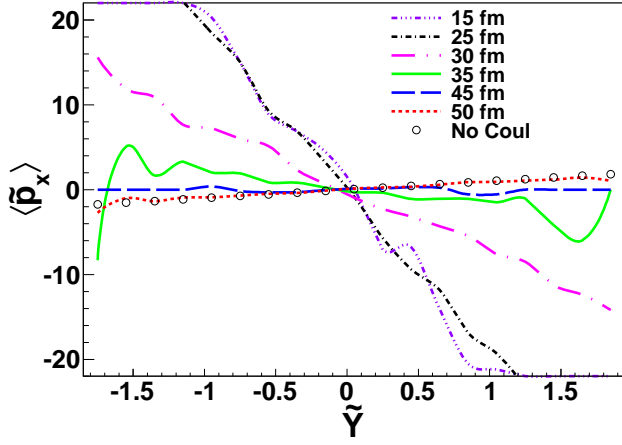


FIG. 14. (color online) Average scaled PLF-plane momentum, $\langle \tilde{p}_x \rangle$, is shown as a function of the scaled rapidity (\tilde{Y}) calculated from the Coulomb trajectory simulation. The proximity of the PLF and TLF to the mid-rapidity particle was varied as described by the legend.

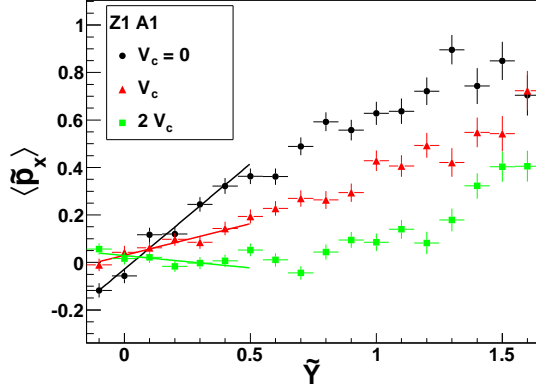


FIG. 15. (color online) Average scaled PLF-plane momentum, $\langle \tilde{p}_x \rangle$, is shown as a function of the scaled rapidity (\tilde{Y}) for protons in correlation with a PLF $Z = 21$ -25 from the filtered CMD simulations at 400 fm/c. The magnitude of the Coulomb potential was varied as described by the legend. A linear fit, represented by the solid colored lines, over the mid-rapidity region is shown for each of the CMD results.

(V_C) from the PLF and TLF on the mid-rapidity region the magnitude of the potential was varied.

In Fig. 15 the $\langle \tilde{p}_x \rangle$ is shown as a function of \tilde{Y} for protons in correlation with PLFs with $Z = 21$ -25. The results show how the repulsive Coulomb potential competes against the attractive nuclear force in determining the trajectories of the mid-rapidity protons. When the Coulomb potential was not used in the CMD simulation ($V_C = 0$), the trajectory of the protons was determined from a combination of nucleon-nucleon collisions and the nuclear force. Without the repulsive Coulomb potential, a relatively large positive slope was extracted from the PLF-scaled flow, as shown by the solid black circles. The magnitude of the slope was decreased when

the Coulomb potential is taken into account in the simulation, as shown by the red triangles. When the strength of the Coulomb potential was doubled, the PLF-scaled flow actually becomes negative.

The CMD results show that the magnitude of the Coulomb potential is strongly connected to the resulting PLF-scaled flow. An increased Coulomb potential caused the particles to be repulsed away from the PLF and TLF producing a negative PLF-scaled flow. In the experimental data, this would imply that the particles which exhibited a negative flow must have felt a stronger Coulomb force than the positive flow particles. Therefore, the observation of a negative PLF-scaled flow should be associated with an early time of emission, since the mid-rapidity particles would have to be in close vicinity to the PLF-TLF. At the later stages of the reaction, the Coulomb field in the mid-rapidity region would not be as strong and therefore, a positive PLF-scaled flow could be observed.

C. Constrained Molecular Dynamics (CoMD)

The constrained molecular dynamics (CoMD) model [45, 46] was used to examine the average order of emission the LCPs in the mid-rapidity region. The dynamical CMD and Coulomb Trajectory simulations provided evidence supporting the idea that the PLF-scaled flow of the LCPs and IMFs is connected to the average order of emission. However, these simulations do not provide a complete description of the heavy-ion collision. The CoMD model includes the nuclear force, Coulomb potential, nucleon-nucleon collisions, and Fermionic nature of the nuclei. The Pauli Principle is accurately described through examining the occupation probability of each nucleon at each time step. The reaction was followed for 3000 fm/c within the CoMD model allowing the system to evolve and cool dynamically. The statistical decay of any remaining hot or unstable fragments after 3000 fm/c was completed with the GEMINI++ code [57, 58]. However, after 3000 fm/c very little excitation energy remained in most fragments.

The production of particles in the mid-rapidity region was studied in reference to the final mid-rapidity yield at $t = \infty$, which is defined as the final distribution calculated after applying GEMINI++. Each event was tagged according to the charge of the PLF at $t = \infty$ and the %Yield defined as

$$\%Yield = \frac{Yield(t = \tau)}{Yield(t = \infty)} \times 100\% \quad (6)$$

was calculated where $Yield(t = \tau)$ represent the yield of a given particle type at some time, τ , and $Yield(t = \infty)$ is the particle yield after the GEMINI++ de-excitation. Therefore, the %Yield represents the relative yield produced at each time step. In Fig. 16 the %Yield, calculated for particles with $0.0 \leq \tilde{Y} \leq 0.45$ (mid-rapidity

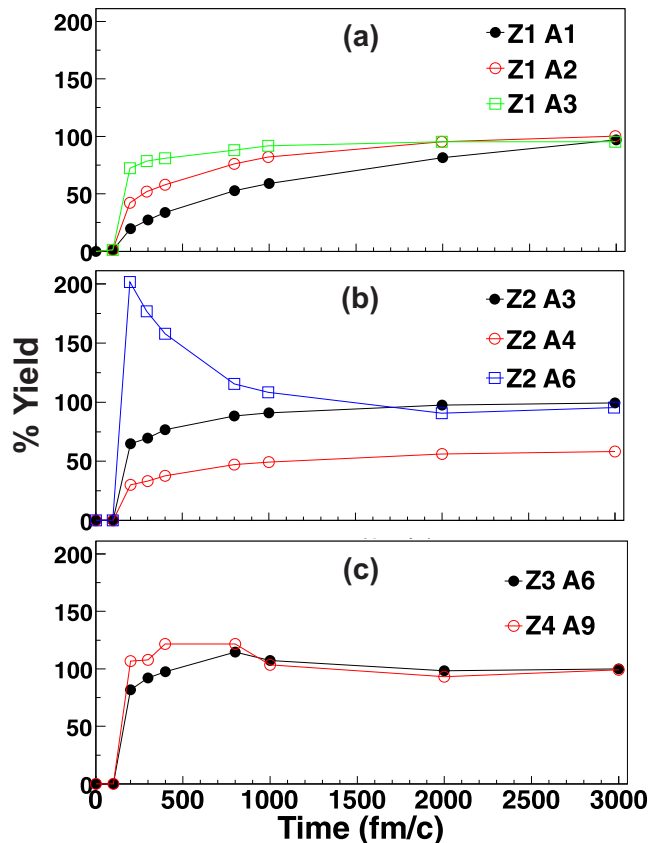


FIG. 16. (color online) Mid-rapidity %Yield as a function of time for different particle types from the CoMD simulation. The results are shown for events in which the final ($t = \infty$) PLF $Z = 21-25$.

region), is shown as a function of time for events in which the final PLF $Z = 20-24$.

The results shown in Fig. 16 are in good agreement with the emission order extracted from the experimental PLF-scaled flow. The %Yield of the $Z = 1$ isotopes, panel (a), shows that a large production of the mid-rapidity tritons occurs relatively early in comparison to the deuterons and protons. The simulation indicates that almost 50% of the mid-rapidity protons are emitted after 1000 fm/c, at which time the proximity of the PLF and TLF should be diminished.

The %Yield results for the $Z = 2$ isotopes, Fig. 16(b), are also in agreement with the emission order determined from the PLF-scaled flow. The mid-rapidity ${}^6\text{He}$ fragments are produced very early in the collision, followed by the ${}^3\text{He}$ fragments and the alpha particles. The ${}^6\text{He}$ fragments show a %Yield greater than 100% at 200 fm/c which represents that some of the produced ${}^6\text{He}$ break-up at a later time steps. Therefore, any ${}^6\text{He}$ that were to reach the detector would likely have had to been produced or formed very early.

The results for the mid-rapidity ${}^6\text{Li}$ and ${}^9\text{Be}$ fragments

(panel (c)), which are the dominant $Z = 3$ and $Z = 4$ isotopes, show a relatively early emission time for the total produced yield. Similar to the ${}^6\text{He}$, the results suggest that some of the ${}^6\text{Li}$ and ${}^9\text{Be}$ fragments break-up at the later stages since the %Yield value increases beyond 100%. Again, this supports the experimental results which suggested that the $Z = 3$ and $Z = 4$ fragments were emitted relatively early and exhibited a PLF-scaled flow similar to the tritons and ${}^6\text{He}$.

Overall, the average emission order from the CoMD model is in good agreement with the experimentally determined emission order from the PLF-scaled flow measurements. The CoMD results depict a scenario in which the mid-rapidity region is preferentially populated with tritons, ${}^6\text{He}$, $Z = 3$, and $Z = 4$ fragments at the early stages of the reaction.

VI. SUMMARY

The correlation of LCPs ($Z = 1-2$) and IMFs ($Z = 3-4$) with PLFs has been investigated for the 35 MeV/nucleon ${}^{70}\text{Zn} + {}^{70}\text{Zn}$, ${}^{64}\text{Zn} + {}^{64}\text{Zn}$, and ${}^{64}\text{Ni} + {}^{64}\text{Ni}$ systems. The flow of the LCPs with respect to the PLF has been studied using the new scaling method presented in Eq. 5 and termed the PLF-scaled flow. The results showed strong correlations between the mid-rapidity LCPs and IMFs with the PLF in the peripheral events.

The magnitude of the PLF-scaled flow, taken as the slope over the mid-rapidity region, was very sensitive to the different $Z = 1$ and $Z = 2$ isotopes. This demonstrated that the different isotopes exhibit different dynamical characteristics. The PLF-scaled flow of the LCPs and IMFs in the mid-rapidity region was suggested to be sensitive to the proximity of the PLF-TLF and therefore, the average order of emission of the mid-rapidity LCPs/IMFs could be obtained. The results indicated that on average the order of emission for the $Z = 1$ isotopes starts with tritons followed by deuterons and then, lastly, protons. The $Z = 2$ isotopes presented an average emission order beginning with the early emission of ${}^8\text{He}$ and ${}^6\text{He}$ followed by ${}^3\text{He}$ and then alpha particles. The $Z = 3$ and $Z = 4$ IMFs showed no significant isotopic effects but showed strong negative PLF-scaled flow indicating a relatively early emission time.

These results depict a scenario in which the mid-rapidity, or neck, region is preferentially populated by the neutron-rich fragments (tritons, ${}^6\text{He}$, ${}^8\text{He}$) and IMFs (at least $Z = 3$ and $Z = 4$) at relatively early stages of the collision. This compliments the recent results of Hudan *et al.* [35] and De Filippo *et al.* [36] which suggest that IMFs with increased N/Z are emitted earlier in the reaction. Thus, it appears the trend of shorter emission times with increasing N/Z is present for both IMFs and LCPs.

A variety of theoretical models and simulations were used to demonstrate the validity of the connection between the PLF-scaled flow and order of emission.

1. The Coulomb trajectory simulation showed that the slope of the PLF-scaled flow is strongly sensitive to the distance between the mid-rapidity particle and the PLF-TLF. A close proximity of the PLF-TLF to the mid-rapidity particle produced a negative PLF-scaled flow.
2. The CMD model demonstrated that the magnitude of the Coulomb force felt by the mid-rapidity particles directly affected the slope of the PLF-scaled flow. In particular, an increased Coulomb potential caused the protons' positive PLF-scaled flow to become negative.
3. The average order of emission of the LCPs/IMFs was extracted from the CoMD model. The extracted average order of emission was in direct agreement with the experimentally obtained emission order from the PLF-scaled flow interpretation.

Together, all the simulations and models provide a consistent picture describing the relationship between the PLF-scaled flow and the order of emission of the LCPs/IMFs.

In conclusion, a new method, the PLF-scaled flow, has been developed to examine the dynamics of the mid-

rapidity LCPs and IMFs in peripheral collisions. The resulting trajectory of the particles, or slope of the PLF-scaled flow, was shown to be sensitive to their average order of emission. The results indicate that the increased neutron enrichment of the neck region is connected to a preferential emission of neutron-rich fragments relatively early in the reaction.

VII. ACKNOWLEDGEMENTS

We would like to thank the staff members of the Texas A&M Cyclotron Institute for the excellent beam quality. This work was supported in part by the Robert A. Welch Foundation through grant No. A-1266, and the Department of Energy through grant No. DE-FG03-93ER40773. We would further like to thank Dr. M. Papa for use of the CoMD code and Dr. R. J. Charity for use of the GEMINI++ code. We would also like to thank the Target Lab at Argonne National Laboratory for the fabrication of the ^{70}Zn target and the Texas A&M Chemistry Supercomputer, National Science Foundation Grant No. CHE-0541587, for time in computing the CoMD calculations.

-
- | | |
|---|---|
| <p>[1] C. P. Montoya <i>et al.</i>, Phys. Rev. Lett. 73, 3070 (1994).
 [2] R. Wada <i>et al.</i>, Nucl. Phys. A548, 471 (1992).
 [3] J. Toke <i>et al.</i>, Nucl. Phys. A583, 519 (1995).
 [4] M. Di Toro, A. Olmi, and R. Roy, Eur. Phys. J. A 30, 65 (2006).
 [5] J. Lukasik <i>et al.</i>, Phys. Rev. C 55, 1906 (1997).
 [6] E. Plagnol <i>et al.</i>, Phys. Rev. C 61, 014606 (1999).
 [7] D. Theriault <i>et al.</i>, Phys. Rev. C 74, 051602(R) (2006).
 [8] J. F. Dempsey <i>et al.</i>, Phys. Rev. C 54, 1710 (1996).
 [9] S. Piantelli <i>et al.</i>, Phys. Rev. C 76, 061601(R) (2007).
 [10] R. Planeta <i>et al.</i>, Phys. Rev. C 77, 014610 (2008).
 [11] S. Hudan <i>et al.</i>, Phys. Rev. C 71, 054604 (2005).
 [12] R. Laforest, E. Ramakrishnan, D. J. Rowland, A. Ruangma, E. M. Winchester, E. Martin, and S. J. Yennello, Phys. Rev. C 59, 2567 (1999).
 [13] D. V. Shetty <i>et al.</i>, Phys. Rev. C 68, 054605 (2003).
 [14] J. Rizzo, M. Colonna, V. Baran, M. Di Toro, H. H. Wolter, and M. Zielinska-Pfabe, Nucl. Phys. A806, 79 (2008).
 [15] R. Lioni, V. Baran, M. Colonna, and M. Di Toro, Phys. Lett. B 625, 33 (2005).
 [16] V. Baran, M. Colonna, M. Di Toro, V. Greco, M. Zielinska-Pfabe, and H. H. Wolter, Nucl. Phys. A703, 603 (2002).
 [17] V. Baran, M. Colonna, and M. Di Toro, Nucl. Phys. A730, 329 (2004).
 [18] L. G. Sobotka, Phys. Rev. C 50, 1272(R) (1994).
 [19] L. Gingras <i>et al.</i>, Phys. Rev. C 65, 061604(R) (2002).
 [20] S. Piantelli, L. Bidini, G. Poggi, M. Bini, G. Casini, P. R. Maurenzig, A. Olmi, G. Pasquali, A. A. Stefanini, and N. Taccetti, Phys. Rev. Lett. 88, 052701 (2002).
 [21] S. Hudan <i>et al.</i>, Phys. Rev. C 70, 031601(R) (2004).
 [22] A. B. McIntosh <i>et al.</i>, Phys. Rev. C 81, 034603 (2010).</p> | <p>[23] R. Ghetti, J. Helgesson, V. Avdeichikov, B. Jakobsson, N. Colonna, G. Tagliente, H. W. Wilschut, and K. V. L., arXiv:nucl-ex/0507029v1 (2005).
 [24] R. Ghetti <i>et al.</i>, Nucl. Phys. A765, 307 (2006).
 [25] G. Verde, A. Chbihi, R. Ghetti, and J. Helgesson, Eur. Phys. J. A 30, 81 (2006).
 [26] C. J. Gelderloos <i>et al.</i>, Phys. Rev. Lett. 75, 3082 (1995).
 [27] Z. Y. He <i>et al.</i>, Eur. Phys. J. A 1, 61 (1998).
 [28] E. W. Cornell <i>et al.</i>, Phys. Rev. Lett. 77, 4508 (1996).
 [29] E. De Flilippo <i>et al.</i>, Phys. Rev. C 71, 044602 (2005).
 [30] G. Casini <i>et al.</i>, Phys. Rev. Lett. 71, 2567 (1993).
 [31] D. Durand <i>et al.</i>, Phys. Lett. B 345, 397 (1995).
 [32] S. Hudan <i>et al.</i>, arXiv:nucl-ex/0308031v2 (2003).
 [33] M. Jandel, A. S. Botvina, S. J. Yennello, G. A. Souliotis, D. V. Shetty, E. Bell, and A. Keksis, J. Phys. G: Nucl. Part. Phys. 31, 29 (2005).
 [34] L. W. Chen, C. M. Ko, and B. A. Li, Nucl. Phys. A729, 809 (2003).
 [35] S. Hudan <i>et al.</i>, Phys. Rev. C 86, 021603 (2012).
 [36] E. D. Flilippo <i>et al.</i>, Phys. Rev. C 86, 014610 (2012).
 [37] S. Wuenschel <i>et al.</i>, Nucl. Instrum. Methods Phys. Res. A 604, 578 (2009).
 [38] R. P. Schmitt <i>et al.</i>, Nucl. Instrum. Methods Phys. Res. A 354, 487 (1995).
 [39] J. Pouthas <i>et al.</i>, Nucl. Instrum. Methods Phys. Res. A 357, 418 (1995).
 [40] K. Kwiatkowski <i>et al.</i>, Nucl. Instrum. Methods Phys. Res. A 360, 571 (1995).
 [41] S. Wuenschel, K. Hagel, L. W. May, R. Wada, and S. J. Yennello, AIP Conf. Proc. 1099, 816 (2009).
 [42] L. Tassan-Got, Nucl. Instrum. Methods Phys. Res. B 194, 503 (2002).
 [43] R. Wada <i>et al.</i>, Phys. Rev. C 69, 044610 (2004).</p> |
|---|---|

- [44] S. Wuenschel, *Temperature and Scaling Studies from Projectile Fragmentation of $^{86,78}\text{Kr}+^{64,58}\text{Ni}$ at 35 MeV/A*, Ph.D. thesis, Texas A&M University (2009).
- [45] M. Papa, T. Maruyama, and A. Bonasera, Phys. Rev. C **64**, 24612 (2001).
- [46] M. Papa, G. Giuliani, and A. Bonasera, J. Comput. Phys. **208**, 403 (2005).
- [47] G. D. Westfall *et al.*, Phys. Rev. Lett. **71**, 1986 (1993).
- [48] B. A. Li, C. M. Ko, and W. Bauer, Int. J. Mod. Phys. **E7**, 147 (1998).
- [49] A. Bonasera and L. P. Csernai, Phys. Rev. Lett. **59**, 630 (1987).
- [50] D. Cussol *et al.*, Phys. Rev. C **65**, 44604 (2002).
- [51] A. Buta *et al.*, Nucl. Phys. A **584**, 397 (1995).
- [52] A. Andronic, J. Lukasik, W. Reisdorf, and W. Trautmann, Eur. Phys. J. A **30**, 31 (2006).
- [53] W. K. Wilson, R. Lacey, C. A. Ogilvie, and G. D. Westfall, Phys. Rev. C **45**, 738 (1992).
- [54] C. A. Ogilvie *et al.*, Phys. Rev. C **40**, 2592 (1989).
- [55] V. Latora, M. Belkacem, and A. Bonasera, Phys. Rev. Lett. **73**, 1765 (1994).
- [56] M. Belkacem, V. Latora, and A. Bonasera, Phys. Rev. C **52**, 271 (1995).
- [57] R. J. Charity *et al.*, Nucl. Phys. **A483**, 371 (1988).
- [58] Charity, R.J., code GEMINI++, (www.chemistry.wustl.edu/rc/gemini++/).